

# Localization of high-entropy metal oxide in iron oxide nanoparticles for efficient oxygen evolution reaction

Liang Qiu<sup>1#</sup>, Baowen Zhou (✉)<sup>1#</sup>, Ying Li<sup>2</sup>, Muhammad Imran Abdullah<sup>2</sup>, Zhaosong Wu<sup>1</sup>, Jianqing Chen<sup>1</sup>, Wanglan Zhou<sup>1</sup>, Tingting Ren<sup>3</sup>, Yuqi Wang<sup>3</sup>, Zhen Huang<sup>1</sup>

<sup>1</sup> Key Laboratory for Power Machinery and Engineering of the Ministry of Education, Research Center for Renewable Synthetic Fuel, School of Mechanical Engineering, Shanghai Jiao Tong University, Shanghai 200240, China

<sup>2</sup> China-UK Low Carbon College, Shanghai Jiao Tong University, Shanghai 201306, China

<sup>3</sup> Institute of Seawater Desalination and Multipurpose Utilization of the Ministry of Natural Resources, Tianjin 300192, China

## HIGHLIGHTS

- A localized high-entropy oxide (LHEO) is spatially confined within  $\alpha\text{-Fe}_2\text{O}_3$  to form a unique nanoarchitecture.
- The catalyst achieves low overpotential (229 mV at 10 mA/cm<sup>2</sup>) and a small Tafel slope (34.4 mV/dec), outperforming RuO<sub>2</sub>.
- Exceptional durability is demonstrated with stable operation over 1000 h and strong performance in seawater-based zinc-air batteries.
- LHEO-induced lattice strain and electronic modulation shift the OER pathway from AEM to LOM, lowering the energy barrier.

### Keywords:

Localized high-entropy engineering  
Earth-abundant oxygen evolution reaction electrocatalysts  
Lattice oxygen mechanism  
Seawater splitting  
Zn-air battery

## ABSTRACT

The development of efficient, durable, and cost-effective oxygen evolution reaction (OER) electrocatalysts is essential for advancing renewable energy technologies. Herein, a novel strategy is reported that spatially confines a nanoscale localized high-entropy oxide (LHEO) consisting of Fe, Co, Ni, Zn, and Mn within  $\alpha\text{-Fe}_2\text{O}_3$ , forming a unique  $\alpha\text{-Fe}_2\text{O}_3\text{@LHEO}$  nanoarchitecture. The catalyst exhibits outstanding OER performance for alkaline water splitting, achieving a current density of 10 mA/cm<sup>2</sup> at a low overpotential of 229 mV with a small Tafel slope of 34.4 mV/dec, significantly outperforming commercial RuO<sub>2</sub> (326 mV, 118.8 mV/dec). It also shows excellent long-term stability over 1000 h at 100 mA/cm<sup>2</sup> without notable activity degradation. Applied in rechargeable zinc-air batteries with natural seawater, the  $\alpha\text{-Fe}_2\text{O}_3\text{@LHEO}$  cathode delivers a high power density of 88.3 mW/cm<sup>2</sup> and stable operation over 600 cycles, substantially surpassing the benchmark Ru-Pt electrocatalyst (74.7 mW/cm<sup>2</sup>, 170 cycles). Combined experimental and theoretical studies reveal that LHEO induces lattice strain in  $\alpha\text{-Fe}_2\text{O}_3$ , modulates its electronic structure, and lowers the crystal field splitting energy to stabilize high-spin Fe<sup>3+</sup>. These effects enhance metallic character for efficient charge transfer and optimize the adsorption/desorption of key oxygen reaction intermediates, thus shifting the OER pathway from the conventional adsorbate evolution mechanism (AEM) to the more energetically favorable lattice oxygen mechanism (LOM) with the energy barrier reduced from 1.85 to 1.71 eV. Overall, this work proposes a novel localized high-entropy engineering approach that overcomes key bottlenecks in designing efficient and durable OER electrocatalysts based on earth-abundant materials.

© The Author(s) 2026.

This article is published with open access at [link.springer.com](http://link.springer.com) and [journal.hep.com.cn](http://journal.hep.com.cn)

## 1 Introduction

The relentless depletion of fossil fuels underscores an urgent need to transition toward a renewable energy

system [1–3]. Central to this transition is the oxygen evolution reaction (OER), a fundamental process in many renewable energy technologies, including water electrolysis for green hydrogen production and metal-air

# These authors contributed equally to this work.

✉ Corresponding author. E-mail: [zhoubw@sjtu.edu.cn](mailto:zhoubw@sjtu.edu.cn)

batteries for energy storage [4–7]. However, OER is inherently hampered by sluggish kinetics, involving a complex four-electron transfer with high energy barriers ( $2\text{H}_2\text{O} \rightarrow \text{O}_2 + 4\text{H}^+ + 4\text{e}^-$ ) [8,9]. Precious metal oxides such as  $\text{IrO}_2$  and  $\text{RuO}_2$  remain the benchmark OER catalysts to overcome these issues. Despite their high activity, their extreme scarcity and unaffordable price—for instance, the global iridium yield is only about 7–8 tons per year—prevent their deployment at the terawatt scales [10,11]. In this context, it is highly desirable to develop high-performance noble-metal-free OER catalysts to break the bottleneck in the renewable energy revolution [12].

Among a variety of non-precious metals, iron-based catalysts have garnered considerable interest owing to their natural abundance, low toxicity, and rich redox chemistry [13–15]. The versatile oxidation states of iron ( $\text{Fe}^{2+}/\text{Fe}^{3+}$ ) support tunable electronic structures well-suited for multi-step reactions such as OER [16]. The adsorption of oxygen-containing intermediates on the catalyst surface is closely related to the spin state of the active metal [17].  $\text{Fe}^{3+}$  exists in three distinct spin states: low-spin (LS,  $t_{2g}^5 e_g^0$ ), intermediate-spin (IS,  $t_{2g}^4 e_g^1$ ), and high-spin (HS,  $t_{2g}^3 e_g^2$ ) [18,19]. High-spin  $\text{Fe}^{3+}$  often plays a significant role in OER reactions [20]. On the one hand, turning the spin-electronic configuration of Fe centers to the high-spin state enables electron penetration into the antibonding  $\pi$ -orbitals of adsorbed species, thereby modulating intermediate adsorption strength [21,22]. On the other hand, high-spin ions can serve as spin channels, enhancing selective extraction of spin-oriented electrons and facilitating the formation of triplet oxygen molecules [23]. However, conventional iron-based catalysts suffer from inherent limitations, including poor electrical conductivity ( $\sim 10^{-14}$  S/cm for  $\alpha\text{-Fe}_2\text{O}_3$ ), suboptimal active-site configurations, and the difficulty in stabilizing high-spin  $\text{Fe}^{3+}$  under operating conditions, all of which hinder the efficient adsorption/desorption of key reaction intermediates and impose significant energy barriers, thereby restricting overall catalytic performance [24]. Recent studies show that tailoring the local chemical environment via doping, defect engineering, and interface structuring can partially enhance catalytic properties [25–27]. Nevertheless, iron-based OER catalysts remain far from practical application.

High-entropy alloys (HEAs), composed of five or more principal elements in near-equimolar ratios, exhibit high configurational entropy and unique electronic and catalytic properties [28–30]. HEA engineering offers a promising route to improve iron-based materials by simultaneously tuning composition, strain, and defects [31–33]. Specifically, lattice distortion induced by atomic size mismatch generates abundant surface defects and

oxygen vacancies, promoting OER pathway toward the lattice oxygen mechanism (LOM) [34,35]. Moreover, HEAs tune the electronic structure and d-band center of iron active sites, optimizing adsorption energies and reducing activation energy barriers [36,37]. Furthermore, the cocktail effect arising from synergistic interactions among multiple elements further enables the integration of complementary functionalities, helping to overcome the activity-stability trade-off that plagues conventional iron-based catalysts [38].

In this study, a localized high-entropy engineering strategy is proposed to improve iron-based OER performance (Fig. 1). A localized high-entropy oxide (LHEO) composed of Fe, Co, Ni, Zn, and Mn is spatially confined within  $\alpha\text{-Fe}_2\text{O}_3$  ( $\alpha\text{-Fe}_2\text{O}_3@\text{LHEO}$ ) for OER catalysis. During water electrolysis,  $\alpha\text{-Fe}_2\text{O}_3@\text{LHEO}$  delivers a low overpotential of 229 mV at 10 mA/cm<sup>2</sup>, with a distinct Tafel slope of 34.4 mV/dec in alkaline electrolyte, substantially outperforming  $\alpha\text{-Fe}_2\text{O}_3$  (299 mV, 61.2 mV/dec) and commercial  $\text{RuO}_2$  (326 mV, 118.8 mV/dec). It exhibits outstanding stability for over 1000 h at 100 mA/cm<sup>2</sup> without significant activity degradation. When applied in a rechargeable Zn–air battery using natural seawater, a high peak power density of 88.3 mW/cm<sup>2</sup> and stable operation over 600 cycles are achieved, surpassing a commercial Ru–Pt catalyst (74.7 mW/cm<sup>2</sup>, 170 cycles). Combined spectroscopic analysis and density functional theory (DFT) calculations reveal that LHEO induces lattice strain, electronic reconfiguration, and stabilization of high spin  $\text{Fe}^{3+}$  in  $\alpha\text{-Fe}_2\text{O}_3$ . This facilitates charge transfer and optimizes intermediate adsorption energies. Meanwhile, the reaction pathway shifts from the adsorbate evolution mechanism (AEM) to the more energetically favorable LOM, with a dramatically reduced energy barrier. This study introduces a nanoscale localized high-entropy engineering strategy for developing efficient, durable, and cost-effective OER electrocatalysts based on earth-abundant materials.

## 2 Method

### 2.1 Working electrode preparation

For the three-electrode configuration, nickel foam (NF) was used as the substrate, with a LHEO/ $\alpha\text{-Fe}_2\text{O}_3$ /carbon nanotubes (CNTs) composite catalytic layer grown *in situ* via a one-step hydrothermal route. Briefly,  $\text{Fe}_2(\text{SO}_4)_3$ ,  $\text{ZnCl}_2$ ,  $\text{CoCl}_2$ ,  $\text{MnSO}_4$ ,  $\text{NiCl}_2$ , and CNTs were weighed at a target molar ratio, dispersed in deionized water (DIW), and stirred until fully dissolved to form a homogeneous precursor solution, followed by ultrasonication for 30 min to ensure uniform dispersion.



cathode with the same loading was prepared.

For the flexible ZAB, the same procedure was followed. A dry polyacrylic acid (PAA) gel was immersed in the electrolyte for 24 h and used as the electrolyte. A well-polished Zn foil served as the anode and was sealed in a plastic bag. After standing for 1 h, electrochemical tests were conducted.

### 3 Characterization

Scanning electron microscopy (SEM) images were obtained on a Quattro ESEM (FEI). Scanning transmission electron microscopy (STEM) imaging was performed on a Thermo Fisher Scientific Talos F200X S/TEM at 200 kV with a Super-energy-dispersive X-ray spectroscopy (EDS) detector. Transmission electron microscopy (TEM) images were obtained using a JEOL 2100F microscope. Electron paramagnetic resonance (EPR) spectra were recorded on a Bruker A300 instrument (Germany). X-ray diffraction (XRD) patterns were obtained using a Bruker D8 Advance diffractometer. X-ray photoelectron spectroscopy (XPS) measurements were conducted on an ESCALAB 250xi system equipped with a non-monochromatic aluminum anode, with the C 1s peak at 284.8 eV used for calibration. Inductively coupled plasma atomic emission spectroscopy (ICP-AES) measurements were conducted using an AGILENT 730 instrument. Vibrating Sample Magnetometer (VSM) were performed using MPMS-VSM at 300 K. Raman spectra were recorded on a HORIBA LabRAM HR Evolution spectrometer, which has a focal length of 800 mm and covers a spectral range from 200 to 3200 nm.

#### 3.1 Electrochemical characterization

All electrochemical tests were performed on a CHI660E electrochemical workstation in a conventional three-electrode system with 1.0 mol/L KOH or 1.0 mol/L KOH + seawater electrolyte (pH 13.6) at  $25 \pm 1$  °C. The working electrode was catalyst-loaded NF, the reference electrode was Hg/HgO (1 mol/L KOH), and the counter electrode was Pt mesh (99.99% purity).

All measured potentials were converted to the reversible hydrogen electrode (RHE) scale using:

$$E_{\text{RHE}} = E_{\text{Hg/HgO}} + 0.0591 \cdot \text{pH} + 0.098 \text{ V.} \quad (1)$$

Linear sweep voltammetry (LSV) was conducted at 10 mV/s from 0.2 to 0.8 V versus RHE. iR compensation (85%) was applied. Tafel slopes were derived using

$$\eta = b \log(j) + a. \quad (2)$$

where  $\eta$  represents the overpotential,  $j$  is the current density, and  $b$  denotes the Tafel slope.

The electrochemical double-layer capacitances ( $C_{\text{dl}}$ ) within the non-Faradaic potential region (1.024–1.224 V versus RHE) were calculated using CV curves recorded at scan rates of 20, 40, 60, 80, 100, and 120 mV/s, and the  $C_{\text{dl}}$  values were obtained by linear fitting the capacitive current differences ( $\Delta j/2$ ) versus scan rate. Electrochemical impedance spectra (EIS) of the catalyst's tests were performed at 10 mA/cm<sup>2</sup> over a frequency window of 10<sup>5</sup>–0.1 Hz. Long-term catalyst durability was assessed via chronopotentiometry (CP) at various current densities.

After assembly, the ZAB was allowed to stand for 12 h. The instantaneous open-circuit potential (OCP) is measured using a multimeter and recorded. Subsequently, a CHI660E workstation was employed to conduct activity and stability tests. The OCP sampling interval was set at 60 s, and the data were monitored and recorded for 10 h. The charge–discharge curves were measured by the LSV method, with a charging range of 1.5–3.2 V, a discharging range of 1.5–0 V, and a scan rate of 10 mV/s. The power density was calculated by the product of the voltage and current of the discharge curve ( $P = U \times I$ ). The specific capacity was determined by constant-current discharging (0.005 A) until battery failure. After recording the mass of the consumed zinc sheet, it was calculated according to  $C = It/m$ . For the cycle stability test, the charge and discharge currents were both set at 5 mA, with each charge and discharge step lasting 600 s. The cycling process was monitored and the data were recorded.

#### 3.2 H<sub>2</sub>O<sub>2</sub> detection

The H<sub>2</sub>O<sub>2</sub> produced during anodic water oxidation was quantified via UV-Vis spectroscopy (Shimadzu UV-3600). Electrocatalytic water oxidation was run in a three-electrode setup at a fixed potential of 1.6 V vs RHE for 30 min. Post-reaction, 1 mL of 1 mol/L HCl was mixed with 3 mL of the reaction solution, then 1 mL of 0.1% OPD solution (chromogenic agent) was added. After complete mixing, the absorption spectrum of the solution was acquired from 300 to 600 nm. The characteristic 438 nm absorption peak of the OPD-H<sub>2</sub>O<sub>2</sub> complex confirmed H<sub>2</sub>O<sub>2</sub> production from water oxidation.

#### 3.3 *In situ* Raman spectroscopy monitoring protocol

Electrochemical Raman spectroscopy (ERS) measurements were conducted using a conventional three-electrode setup under potentiostatic regulation. The active

working electrode was sequentially polarized at potentials ranging from the open-circuit potential (OCP) to 0.8 V versus RHE in 0.1 V increments. For every applied potential, chronoamperometric ( $i-t$ ) measurements were recorded for 300 s. Raman spectra were acquired after a 5-min stabilization period to minimize transient interfacial effects. Each potential step was replicated 1–2 times to mitigate the adverse impacts of random signal fluctuations and gas bubble formation during testing.

### 3.4 Computational detail

DFT [39] calculations were performed using the Vienna Ab Initio Simulation Package (VASP) [40,41]. The interaction between valence electrons and ionic cores was described by the projector-augmented wave (PAW) method [42,43]. Exchange-correlation effects within the Kohn-Sham framework were treated using the Perdew-Burke-Ernzerhof (PBE) functional under the generalized gradient approximation (GGA) [44]. A plane-wave basis set with a kinetic energy cutoff of 400 eV was used to expand the wave functions. Due to the relatively large system and sampling size, only the  $\Gamma$  k-point is sampled in the Brillouin zone [45].

Geometry optimization was performed with convergence criteria of 0.02 eV/Å for atomic forces and  $10^{-4}$  eV for total energy, while a stricter criterion of  $10^{-6}$  eV was applied for precise energy calculations. During structural relaxation, the bottom two atomic layers were fixed at their bulk positions in the slab models. To avoid interactions between periodic images, a vacuum layer of at least 25 Å was introduced perpendicular to the surface for all slabs and in all three spatial dimensions for nanoclusters.

The Gibbs free energy of adsorption ( $\Delta G$ ) was calculated using

$$\Delta G = E_{\text{ad}} + \Delta ZPE - T\Delta S, \quad (3)$$

where  $E_{\text{ad}}$  is the adsorption energy defined by

$$E_{\text{ad}} = E_{\text{surface+adsorbate}} - E_{\text{surface}} - E_{\text{adsorbate}}. \quad (4)$$

$\Delta ZPE$  and  $\Delta S$  are the changes in zero-point energy and entropy during adsorption [46,47].

## 4 Results and discussion

A LHEO composed of Fe, Co, Ni, Zn, and Mn was incorporated into  $\alpha$ -Fe<sub>2</sub>O<sub>3</sub> via a one-step hydrothermal method (see Experimental Section and Fig. S1). SEM shows that the  $\alpha$ -Fe<sub>2</sub>O<sub>3</sub>@LHEO nanoarchitecture is firmly anchored on the nickel foam substrate (Fig. S2). Contact angle measurements indicate a transition from

hydrophobic to hydrophilic behavior with gas-repellent properties (Fig. S3), facilitating rapid bubble release during water electrolysis.

STEM reveals  $\alpha$ -Fe<sub>2</sub>O<sub>3</sub>@LHEO nanoparticles with an average size of approximately 50 nm (Fig. 2(a)). EDX mapping confirms homogeneous dispersion of the LHEO phase within  $\alpha$ -Fe<sub>2</sub>O<sub>3</sub> (Fig. 2(b)). ICP-AES indicates Fe as the main component, while the other four elements exhibit similar contents (Fig. S4). Fast Fourier transform (FFT) analysis identifies the [001] zone axis, corresponding to the exposed (001) plane of  $\alpha$ -Fe<sub>2</sub>O<sub>3</sub> (Fig. 2(c)) [48,49].

Aberration-corrected TEM (AC-TEM) further confirms the coexistence of LHEO and  $\alpha$ -Fe<sub>2</sub>O<sub>3</sub> (Figs. 2(d) and 2(e)). Notably, the LHEO region exhibits higher 3D intensity, attributed to severe lattice distortion induced by the high-entropy effect. Well-defined lattice fringes with a spacing of 0.252 nm correspond to the (110) plane of  $\alpha$ -Fe<sub>2</sub>O<sub>3</sub>, while a reduced lattice spacing of 0.247 nm in the LHEO region indicates lattice contraction (Figs. 2(e) and 2(f)). EPR spectra reveal a significantly enhanced oxygen vacancy signal, evidencing that the LHEO induces substantial lattice strain and promotes oxygen vacancy formation (Fig. 2(g)).

XRD confirms that  $\alpha$ -Fe<sub>2</sub>O<sub>3</sub>@LHEO retains the hematite R3c structure ( $\alpha$ -Fe<sub>2</sub>O<sub>3</sub>,  $a = b = 5.037$  Å,  $c = 13.771$  Å,  $\alpha = \beta = 90^\circ$ ,  $\gamma = 120^\circ$ ) (JCPDS 89-0596), with no additional peaks observed (Fig. S5), indicating phase compatibility. XPS reveals a positive shift of 0.81 eV in the Fe 2p in  $\alpha$ -Fe<sub>2</sub>O<sub>3</sub>@LHEO compared to pristine  $\alpha$ -Fe<sub>2</sub>O<sub>3</sub> and an increased Fe<sup>3+</sup> (Figs. 2(h), S6). Additionally, the O 1s peak of pristine  $\alpha$ -Fe<sub>2</sub>O<sub>3</sub> shifts from 529.3 to 530.2 eV after LHEO incorporation (Fig. 2(i)). The presence of Co, Cr, Zn, and Mn is also confirmed (Fig. S7). These results verified successful nanoscale localization of high-entropy oxide in  $\alpha$ -Fe<sub>2</sub>O<sub>3</sub>, and strong electronic interactions with  $\alpha$ -Fe<sub>2</sub>O<sub>3</sub>.

DFT calculations were conducted to study the structural and electronic properties of the electrocatalysts. The introduction of LHEO induces lattice distortion in  $\alpha$ -Fe<sub>2</sub>O<sub>3</sub>, as reflected by a reduced average Fe–O bond length (1.91 Å in  $\alpha$ -Fe<sub>2</sub>O<sub>3</sub>@LHEO versus 1.93 Å in pristine  $\alpha$ -Fe<sub>2</sub>O<sub>3</sub>; Fig. 3(a)). Charge density difference and Bader charge analysis (Fig. 3(b) and Table S1) reveal electron transfer from  $\alpha$ -Fe<sub>2</sub>O<sub>3</sub> to LHEO, lowering the average Bader charge on both Fe and O sites in  $\alpha$ -Fe<sub>2</sub>O<sub>3</sub>@LHEO. This charge redistribution signifies an increased oxidation state of Fe, which is corroborated by the electronic density of states (DOS). The total DOS shows an elevated number of occupied states near the Fermi level in  $\alpha$ -Fe<sub>2</sub>O<sub>3</sub>@LHEO, indicating enhanced electrical conductivity, which is conducive to rapid electron transfer during electrocatalysis (Fig. S8).

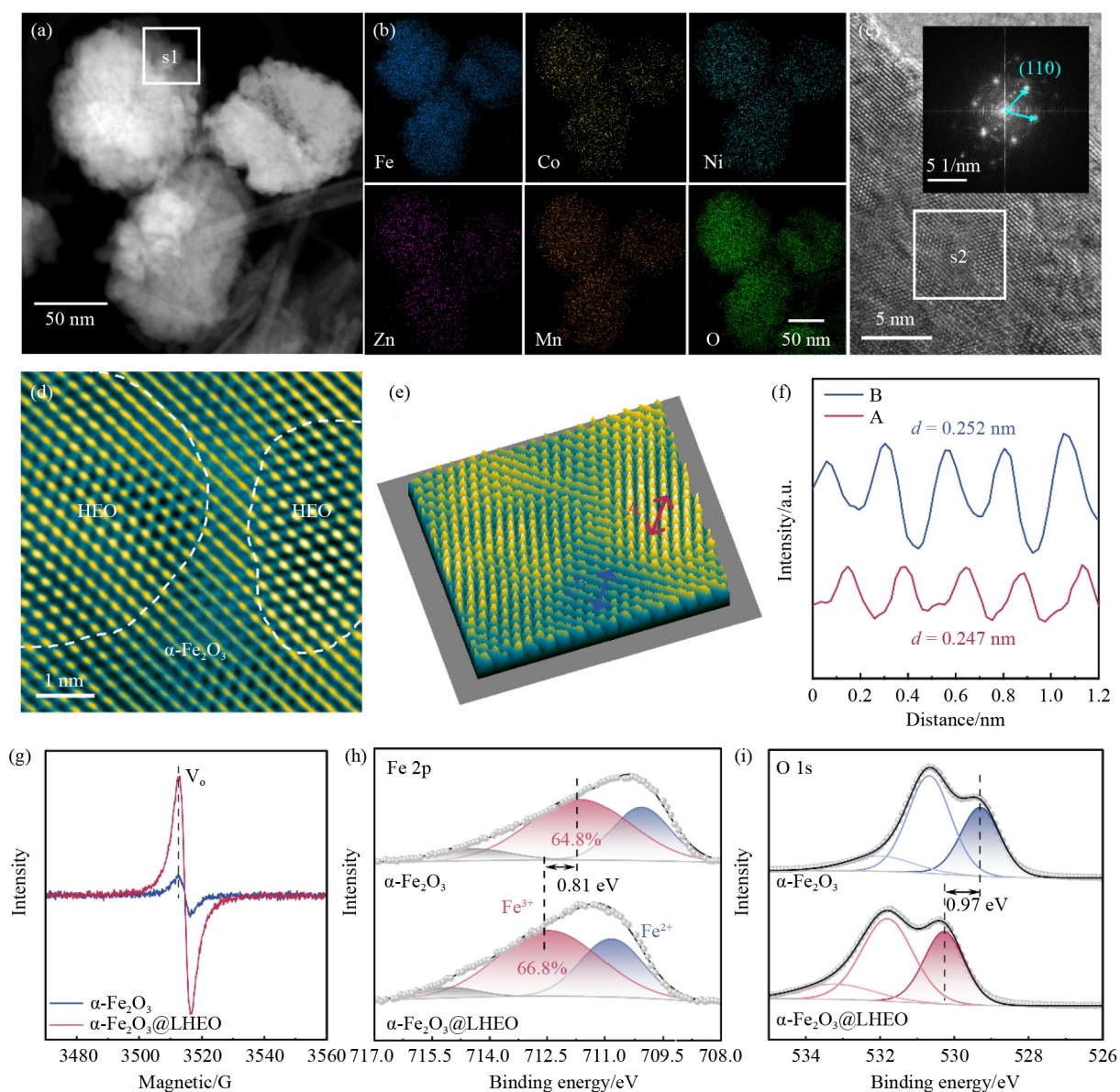


**Fig. 2** Synthesis and characterization of  $\alpha\text{-Fe}_2\text{O}_3\text{@LHEO}$ .

(a) STEM; (b) EDS elemental mapping images of  $\alpha\text{-Fe}_2\text{O}_3\text{@LHEO}$ ; (c) AC-TEM image of  $\alpha\text{-Fe}_2\text{O}_3\text{@LHEO}$  and the corresponding FFT transformation; (d) high-resolution AC-TEM image of  $\alpha\text{-Fe}_2\text{O}_3\text{@LHEO}$ ; (e) 3D surface intensity; (f) atom intensity line in (e); (g) EPR patterns of  $\alpha\text{-Fe}_2\text{O}_3\text{@LHEO}$  and  $\alpha\text{-Fe}_2\text{O}_3$ ; (h) high-resolution XPS spectra of Fe 2p; (i) high-resolution XPS spectra of O 1s in  $\alpha\text{-Fe}_2\text{O}_3\text{@LHEO}$  and  $\alpha\text{-Fe}_2\text{O}_3$ .

More critically, projection of the DOS onto the Fe-3d orbitals reveals a downshift of the Fe d-band center from  $-1.51$  eV in pristine  $\alpha\text{-Fe}_2\text{O}_3$  to  $-1.63$  eV in  $\alpha\text{-Fe}_2\text{O}_3\text{@LHEO}$  (Fig. 3(c)). This shift results from increased nuclear attraction upon electron loss, which contracts the d orbitals. This lowered d-band center is favorable for weakening the adsorption strength of oxygenated intermediates on the catalyst surface. It thereby lowers the energy barrier of the potential-determining step in the OER, as further discussed below.

Crystal field theory provides additional insight into this electronic regulation. The crystal field splitting energy ( $\Delta_0$ ) decreases significantly from  $\Delta_0 = 0.106$  eV in  $\alpha\text{-Fe}_2\text{O}_3$  to  $0.087$  eV in  $\alpha\text{-Fe}_2\text{O}_3\text{@LHEO}$  (Figs. 3(d), S9). A smaller  $\Delta_0$  favors a high-spin state of  $\text{Fe}^{3+}$  ions (Fig. 3(e)) by promoting electron occupation of higher-energy orbitals rather than spin pairing [50]. This is supported by room-temperature magnetic hysteresis (M-H) loop combined with EPR results (Figs. 2(g), S10) [51–53]. This high-spin state results in a larger ionic radius of

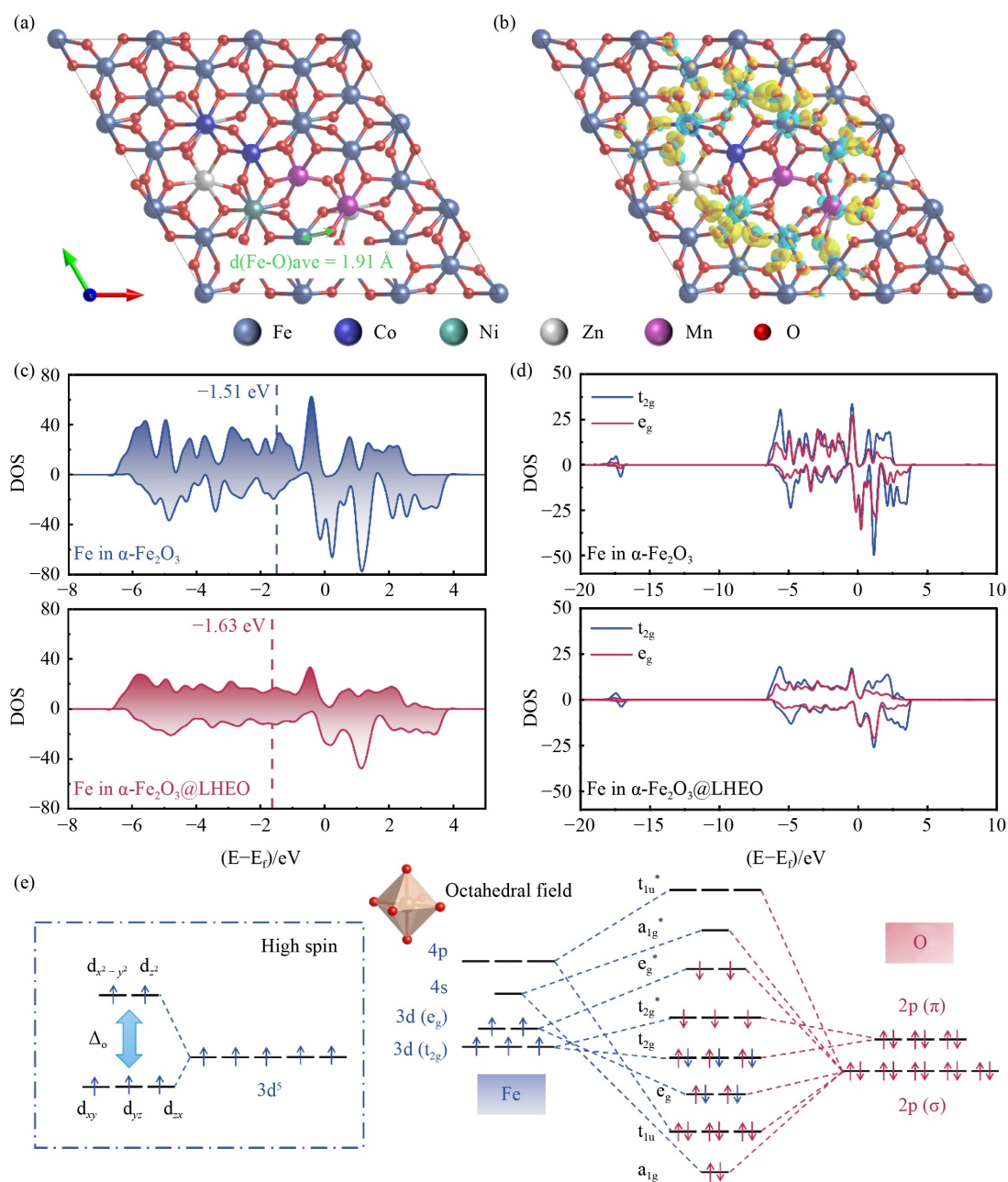


**Fig. 3** Theoretical investigations of the electronic/molecular structure of  $\alpha\text{-Fe}_2\text{O}_3\text{@LHEO}$ .

(a) Optimized structures; (b) charge density of  $\alpha\text{-Fe}_2\text{O}_3\text{@LHEO}$  (yellow representing electron accumulation, blue represents electron depletion); (c) PDOS profile on Fe orbitals of  $\alpha\text{-Fe}_2\text{O}_3\text{@LHEO}$  and pure  $\alpha\text{-Fe}_2\text{O}_3$ ; (d) PDOS on the spin orbitals of  $t_{2g}$  and  $e_g$  of Fe atoms; (e) crystal field and electronic structure of  $\text{FeO}_6$  with high-spin  $\text{Fe}^{3+}$ .

$\text{Fe}^{3+}$ , providing a fundamental explanation for the observed lattice contraction [54–56].

Overall, localized high-entropy engineering not only downshifts the Fe d-band center to optimize intermediate adsorption but also introduces defects that significantly enhance the intrinsic conductivity of the material, thereby synergistically contributing to the exceptional OER catalytic performance, as discussed below.

#### 4.1 Electrocatalytic water splitting performance of $\alpha\text{-Fe}_2\text{O}_3\text{@LHEO}$

The OER performance of water electrolysis over  $\alpha\text{-Fe}_2\text{O}_3\text{@LHEO}$  was first evaluated in 1.0 mol/L KOH aqueous solution using a standard three-electrode configuration (Figs. S11 and S12). The iR-corrected LSV curves were collected at a scan rate of 10 mV/s. As shown in

Fig. 4(a), the overpotential ( $\eta$ ) of  $\alpha$ -Fe<sub>2</sub>O<sub>3</sub>@LHEO is markedly lower than that of commercial RuO<sub>2</sub>. Specifically, the overpotentials of  $\alpha$ -Fe<sub>2</sub>O<sub>3</sub>@LHEO at current densities of 10 and 100 mA/cm<sup>2</sup> were measured to be 229 and 306 mV, respectively. Meanwhile, the corresponding Tafel slope of  $\alpha$ -Fe<sub>2</sub>O<sub>3</sub>@LHEO is as low as 34.4 mV/dec, substantially lower than that of RuO<sub>2</sub> (118.8 mV/dec), indicating accelerated OER kinetics (Fig. 4(b)).

To elucidate the origin of the exceptional performance, the electrochemical active surface area (ECSA) was determined via  $C_{dl}$  measurements in the non-Faradaic region (1.024–1.224 V versus RHE; Fig. S13). The  $C_{dl}$  of  $\alpha$ -Fe<sub>2</sub>O<sub>3</sub>@LHEO is 6.8 mF/cm<sup>2</sup>, significantly higher than

those of  $\alpha$ -Fe<sub>2</sub>O<sub>3</sub> (4.7 mF/cm<sup>2</sup>) and RuO<sub>2</sub> (4.2 mF/cm<sup>2</sup>) (Fig. 4(c)), corresponding to an ECSA of 85 cm<sup>2</sup> (Table S2). This large active area provides abundant reaction sites for catalysis. Furthermore, ECSA-normalized polarization curves (Fig. S14) show that, at a given overpotential, the current density of  $\alpha$ -Fe<sub>2</sub>O<sub>3</sub>@LHEO is significantly higher than that of  $\alpha$ -Fe<sub>2</sub>O<sub>3</sub>. This result confirms that the enhanced catalytic performance of  $\alpha$ -Fe<sub>2</sub>O<sub>3</sub>@LHEO arises not only from increased active sites but also from enhanced intrinsic activity per site. EIS measurements reveal a lower charge-transfer resistance for  $\alpha$ -Fe<sub>2</sub>O<sub>3</sub>@LHEO compared to  $\alpha$ -Fe<sub>2</sub>O<sub>3</sub> and RuO<sub>2</sub> (Fig. 4(d)). This finding is in excellent agreement with the DFT results above, suggesting facilitated charge

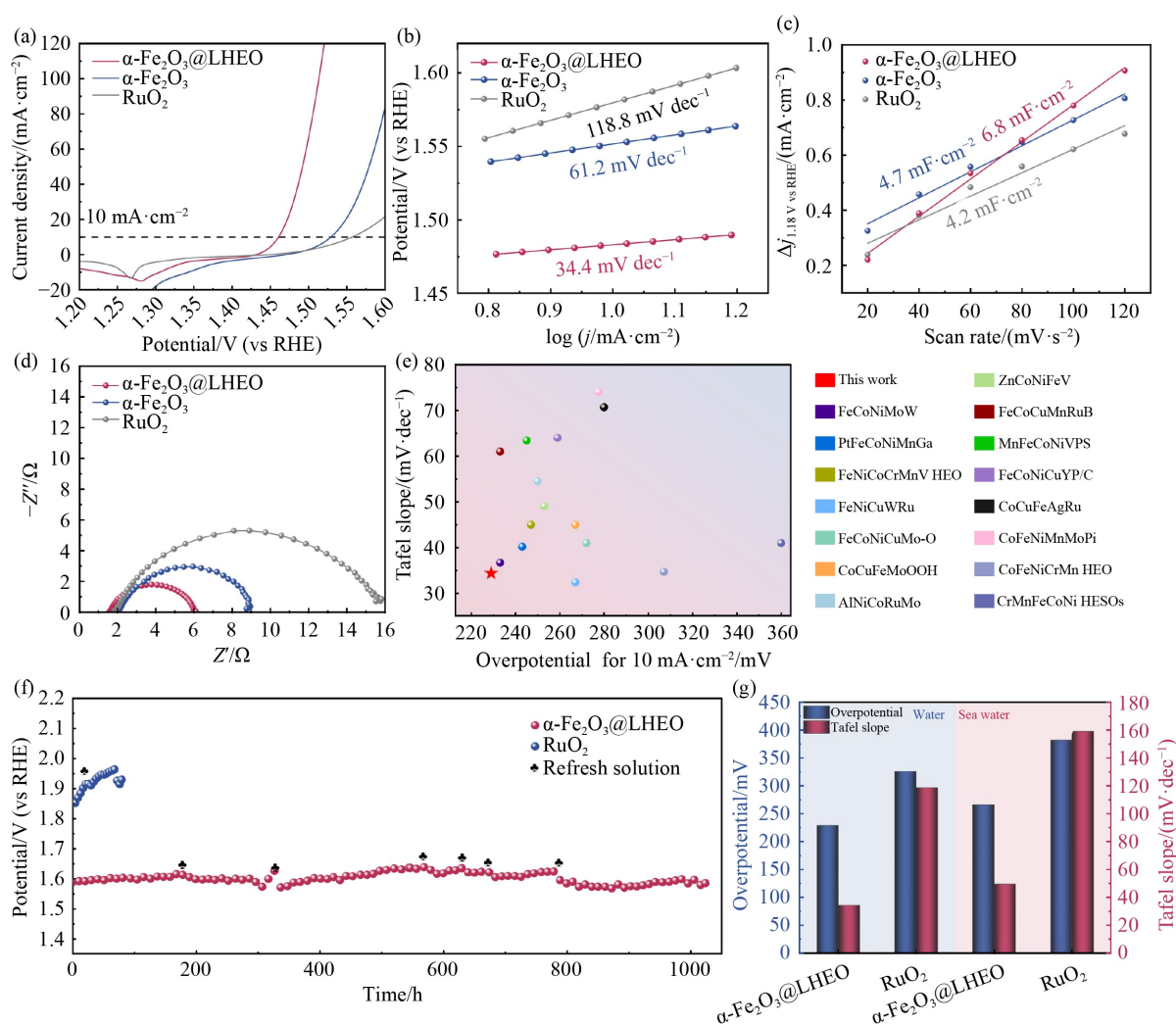


**Fig. 4** OER performance in alkaline electrolyte for water/seawater electrolysis.

(a) LSV curves of  $\alpha$ -Fe<sub>2</sub>O<sub>3</sub>@LHEO,  $\alpha$ -Fe<sub>2</sub>O<sub>3</sub>, and commercial RuO<sub>2</sub>; (b) Tafel slopes of different OER catalysts measured at a scan rate of 10 mV/s; (c) capacitive current density as a function of the scan rate; (d) EIS measurements for  $\alpha$ -Fe<sub>2</sub>O<sub>3</sub>,  $\alpha$ -Fe<sub>2</sub>O<sub>3</sub>@LHEO, and RuO<sub>2</sub>; (e) summary of high entropy catalysts for OER in alkaline water; (f)  $v$ - $t$  curves at the current densities of 100 mA/cm<sup>2</sup>; (g) performance summary of different electrocatalysts at 10 mA/cm<sup>2</sup>.

transfer upon the introduction of LHEO.

Compared with recently reported high-entropy OER electrocatalysts, the alkaline OER catalyst presented in this work demonstrates superior performance (Fig. 4(e) and Table S3). Notably,  $\alpha\text{-Fe}_2\text{O}_3\text{@LHEO}$  suppresses the formation of  $\text{H}_2\text{O}_2$  compared to  $\alpha\text{-Fe}_2\text{O}_3$ , as revealed by UV-Vis spectroscopy (Fig. S15 and S16). In addition,  $\alpha\text{-Fe}_2\text{O}_3\text{@LHEO}$  exhibits excellent stability, maintaining operation for nearly 1000 h at a high current density of  $100\text{ mA/cm}^2$ , highlighting its potential for storing renewable electricity as green  $\text{H}_2$  without noble metals (Fig. 4(f)). After the stability test, no collapse of the NF framework or detachment of  $\alpha\text{-Fe}_2\text{O}_3\text{@LHEO}$  was observed (Figs. S17–S19).

To broaden its applicability, the catalyst was also evaluated for OER in natural seawater electrolyte (Fig.

S20 and Table S4). As illustrated in Figs. 4(g) and S21,  $\alpha\text{-Fe}_2\text{O}_3\text{@LHEO}$  maintains a substantial overpotential advantage over  $\text{RuO}_2$  and exhibits faster OER kinetics in natural seawater, as reflected by a lower Tafel slope ( $49.5\text{ mV/dec}$ ; Fig. S22). The measured  $C_{\text{dl}}$  value of  $\alpha\text{-Fe}_2\text{O}_3\text{@LHEO}$  ( $5.2\text{ mF/cm}^2$ ) is 1.79 times that of  $\text{RuO}_2$  ( $2.9\text{ mF/cm}^2$ ) (Figs. S23 and S24). Meanwhile,  $\alpha\text{-Fe}_2\text{O}_3\text{@LHEO}$  shows more efficient charge transfer in seawater (Fig. S25). These results demonstrate that localized high-entropy oxides in  $\alpha\text{-Fe}_2\text{O}_3$  serve as a promising alternative to noble metals as efficient and stable OER electrocatalysts for both water and seawater electrolysis.

To further investigate the origin of the exceptional catalytic performance, the pH-dependent OER activity was measured (Fig. 5(a)) [57]. The significantly stronger

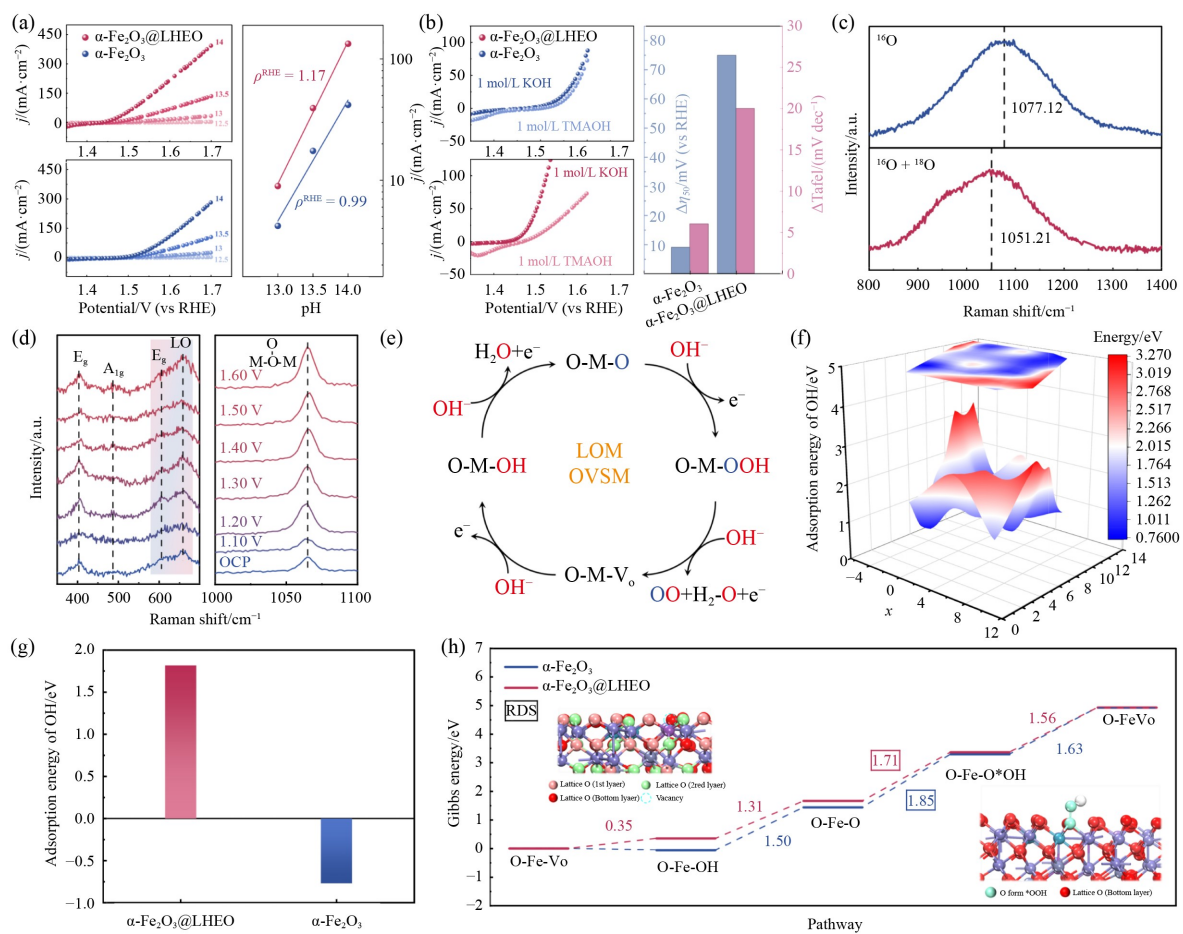


**Fig. 5** OER mechanism investigation.

(a) pH-dependent OER performance of  $\alpha\text{-Fe}_2\text{O}_3\text{@LHEO}$  and  $\alpha\text{-Fe}_2\text{O}_3$ ; (b) OER test using TMAOH as molecular probe over  $\alpha\text{-Fe}_2\text{O}_3\text{@LHEO}$  and  $\alpha\text{-Fe}_2\text{O}_3$ ; (c) *in situ* Raman spectroscopic characterizations under applied potential over  $\alpha\text{-Fe}_2\text{O}_3\text{@LHEO}$  with and without  $\text{H}_2^{18}\text{O}$ ; (d) *in situ* Raman spectra of  $\alpha\text{-Fe}_2\text{O}_3\text{@LHEO}$  under different applied potentials; (e) schematic illustration of the LOM pathway; (f) calculated potential energy surface for \*OH adsorption on metal sites of  $\alpha\text{-Fe}_2\text{O}_3\text{@LHEO}$ ; (g) comparison of \*OH adsorption energies on metal sites for  $\alpha\text{-Fe}_2\text{O}_3\text{@LHEO}$  and  $\alpha\text{-Fe}_2\text{O}_3$ ; (h) Gibbs free energy diagram of the OER pathway over  $\alpha\text{-Fe}_2\text{O}_3\text{@LHEO}$  and  $\alpha\text{-Fe}_2\text{O}_3$ .

pH dependence of the OER rate (higher  $j$  versus pH slope) for  $\alpha\text{-Fe}_2\text{O}_3\text{@LHEO}$  is consistent with the proton-electron non-concerted transfer feature of the LOM pathway, which is distinctly different from the AEM behavior of pristine  $\alpha\text{-Fe}_2\text{O}_3$ . The OER performance of  $\alpha\text{-Fe}_2\text{O}_3\text{@LHEO}$  was further tested in 1 mol/L TMAOH (Fig. S26), showing significantly reduced OER activity and slower kinetics compared to those in 1 mol/L KOH (Fig. 5(b)) [58]. This is attributed to  $\text{TMA}^+$  consuming surface  $\text{O}_2^{2-}/\text{O}^{2-}$  active species, thereby suppressing the LOM-OER process. These results confirm that the reaction pathway shifts from AEM to LOM upon the introduction of localized high-entropy oxides in  $\alpha\text{-Fe}_2\text{O}_3$ .

Surface Raman spectroscopy (SRS) characterization was performed to gain deeper insight into the reaction mechanism using  $^{18}\text{O}$ -labeled  $\text{H}_2\text{O}$ . As illustrated in Fig. 5(c), the characteristic peak at  $1050\text{--}1100\text{ cm}^{-1}$  is assigned to the metal-oxygen (M–O) stretching vibration. Notably, this peak in the isotopically labeled  $\text{H}_2^{18}\text{O}$  electrolyte exhibits a negative shift from  $1077.12\text{ cm}^{-1}$  to  $1051.21\text{ cm}^{-1}$  compared to  $\text{H}_2\text{O}$ . This shift is attributed to the substitution of lattice  $\text{M}\text{-}^{16}\text{O}$  with  $\text{M}\text{-}^{18}\text{O}$  [59]. These observations provide strong evidence that the LOM dominates OER catalysis over  $\alpha\text{-Fe}_2\text{O}_3\text{@LHEO}$ .

Further investigation was performed using *in situ* Raman spectroscopy under varying applied potentials (Fig. 5(d)). In the transverse optical (TO) region, one spectral peak at  $\sim 490\text{ cm}^{-1}$  is assigned to the symmetric  $A_{1g}$  mode, while two additional peaks at  $\sim 410$  and  $\sim 610\text{ cm}^{-1}$  correspond to doubly degenerate  $E_g$  modes. An additional peak at  $660\text{ cm}^{-1}$  is observed, which can be ascribed to the relaxation of longitudinal optical (LO) phonon selection rules induced by oxygen vacancies [60]. The intensity ratio of the LO mode to the  $E_g$  mode ( $I[\text{LO}]/I[E_g]$ ) was employed to quantify variation in oxygen vacancy content [61]. As illustrated in Fig. S27, the oxygen vacancy concentration exhibits a fluctuating upward trend with increasing applied potential, indicating a dynamic generation-consumption cycle during the OER. Additionally, the peak located at  $\sim 1070\text{ cm}^{-1}$  is assigned to bridging peroxide species (M–O<sub>2</sub>–M), whose intensity increases progressively with increasing applied potential. Combined with the EPR results (Fig. 2(g)), these findings indicate that the reaction pathway shifts from AEM in  $\alpha\text{-Fe}_2\text{O}_3$  to LOM in  $\alpha\text{-Fe}_2\text{O}_3\text{@LHEO}$  (Fig. 5(e)).

DFT calculations were further conducted to elucidate the reaction mechanism at the atomic scale. Since the characteristic step of AEM involves OH adsorption on metal sites, a potential energy surface based on OH adsorption free energies was constructed for  $\alpha\text{-Fe}_2\text{O}_3\text{@LHEO}$  (Figs. 5(f) and S28). As shown in Fig. 5(g), OH adsorption on pristine  $\alpha\text{-Fe}_2\text{O}_3$  exhibits negative

adsorption energy, indicating that the formation of Fe–OH intermediates is energetically favorable in the absence of LHEO. This further supports the role of LHEO in shifting the mechanism from AEM to LOM.

The OER pathways over  $\alpha\text{-Fe}_2\text{O}_3\text{@LHEO}$  and  $\alpha\text{-Fe}_2\text{O}_3$  were further calculated (Figs. 5(h), S29 and S30). The reaction initiates at abundant surface oxygen vacancies, where a solution-phase  $\text{OH}^-$  fills an oxygen vacancy and undergoes deprotonation. Subsequently, OH is adsorbed onto a lattice oxygen site to form a Fe–OOH intermediate, followed by deprotonation of OOH and regeneration of oxygen vacancy. The OOH deprotonation step ( $\text{O-Fe-OOH} + \text{OH}^- \rightarrow \text{O-Fe-OO} + \text{H}_2\text{O} + \text{e}^-$ ) is identified as the rate-determining step (RDS). Notably, the introduction of LHEO lowers the energy barrier of the RDS from 1.85 to 1.71 eV.

## 4.2 Rechargeable ZAB

To broaden the application,  $\alpha\text{-Fe}_2\text{O}_3\text{@LHEO}$  was employed as the air electrode (catalyst loading:  $0.25\text{ mg/cm}^2$ ) in a rechargeable ZAB, with commercial Pt/C serving as the cathode (Fig. S31). The battery was assembled in a layered configuration (Fig. S32) and tested in a 6 mol/L KOH-natural seawater electrolyte containing 0.20 mol/L  $\text{Zn}(\text{Ac})_2$ , using a 0.3 mm thick zinc plate as the anode. The  $\alpha\text{-Fe}_2\text{O}_3\text{@LHEO} + \text{Pt/C}$  based ZAB achieved an open-circuit potential of 1.415 V, surpassing that of  $\text{RuO}_2 + \text{Pt/C}$  (1.349 V) (Fig. 6(a)). As shown in Fig. 6(b), it also delivered a higher peak power density of  $88.3\text{ mW/cm}^2$ , compared to  $74.7\text{ mW/cm}^2$  for the  $\text{RuO}_2 + \text{Pt/C}$  counterpart. At a current density of  $5\text{ mA/cm}^2$ , the specific discharge capacity of  $\alpha\text{-Fe}_2\text{O}_3\text{@LHEO} + \text{Pt/C}$  reached  $819.9\text{ mAh/g}_{\text{Zn}}$  (Figs. 6(c) and S33), exceeding the  $790.9\text{ mAh/g}_{\text{Zn}}$  obtained with  $\text{RuO}_2 + \text{Pt/C}$ . Long-time cycling tests at  $5\text{ mA/cm}^2$  further confirmed the superior stability of the  $\alpha\text{-Fe}_2\text{O}_3\text{@LHEO} + \text{Pt/C}$  system (Figs. 6(d) and 6(e)).

It exhibited initial charge/discharge voltages of 2.08 V and 1.14 V, respectively, yielding a voltage gap ( $\Delta E$ ) of 0.93 V, and a corresponding round-trip efficiency of 54.8%. After 600 cycles, the voltage gap increased by only 1.07 mV. In contrast, the  $\text{RuO}_2 + \text{Pt/C}$  battery, although showing a slightly higher initial efficiency of 56.7% (charge: 2.06 V, discharge: 1.17 V), suffered from rapid degradation, with the voltage gap widening to 1.30 V after only 170 cycles. These results highlight the markedly improved energy conversion efficiency and cycling durability of the  $\alpha\text{-Fe}_2\text{O}_3\text{@LHEO}$ -based electrode.

Given the growing promise of all-solid-state ZAB as efficient and sustainable power sources, a flexible all-solid-state ZAB (F-ZAB) was further fabricated. The

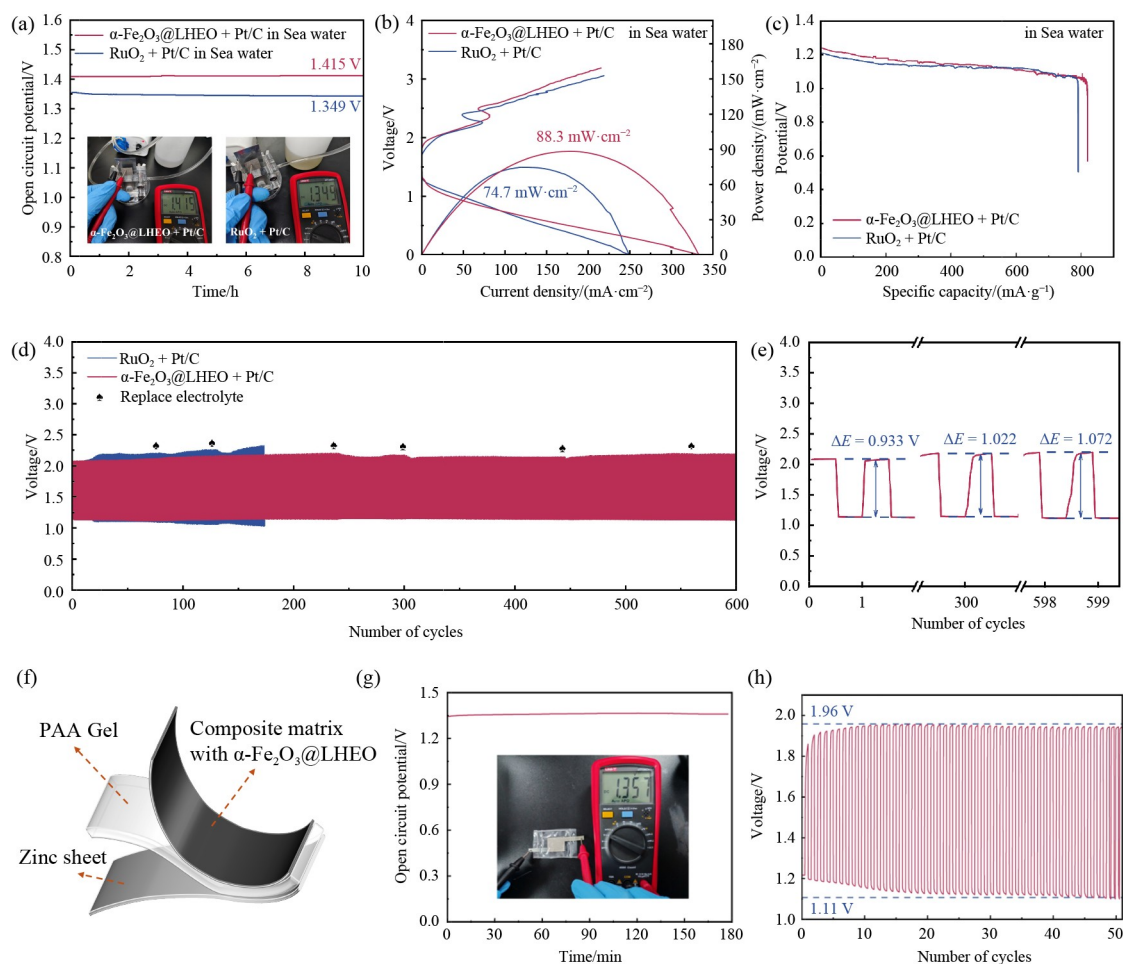


**Fig. 6** Rechargeable ZAB performance in natural seawater.

(a) Open circuit voltage curves for 10 h and digital photos of  $\alpha\text{-Fe}_2\text{O}_3\text{@LHEO} + \text{Pt/C}$  and  $\text{RuO}_2 + \text{Pt/C}$  based Zn-air batteries; (b) polarization curves of  $\alpha\text{-Fe}_2\text{O}_3\text{@LHEO} + \text{Pt/C}$  and  $\text{RuO}_2 + \text{Pt/C}$ , and their corresponding power density curves; (c) specific discharge capacity of  $\alpha\text{-Fe}_2\text{O}_3\text{@LHEO} + \text{Pt/C}$  and  $\text{RuO}_2 + \text{Pt/C}$  at a current density of  $5 \text{ mA/cm}^2$ ; (d, e) charge-discharge cycle curves; (f) schematic illustration of the flexible rechargeable ZAB with  $\alpha\text{-Fe}_2\text{O}_3\text{@LHEO} + \text{Pt/C}$  couple as the air cathode electrocatalyst; (g) open circuit voltage curves for 180 min and digital photo of  $\alpha\text{-Fe}_2\text{O}_3\text{@LHEO} + \text{Pt/C}$  based F-ZAB to show open-circuit potential; (h) charge-discharge cycle.

device consists of a nickel-foam-supported  $\alpha\text{-Fe}_2\text{O}_3\text{@LHEO} + \text{Pt/C}$  integrated electrode as the air cathode, a natural-seawater-soaked alkaline polyacrylic acid (PAA) gel as the electrolyte, and a Zn foil as the anode (Fig. 6(f)). The assembled F-ZAB achieved an open-circuit voltage of 1.36 V (Fig. 6(g)) and delivered a high power density of  $36.4 \text{ mW/cm}^2$  (Fig. S34). During galvanostatic cycling at  $5.0 \text{ mA/cm}^2$ , it exhibited stable charge and discharge voltages of 1.96 and 1.11 V, respectively (Fig. 6(h)). The resulting  $\Delta E$  of 0.85 V corresponds to a round-trip efficiency of 56.6%, and the battery maintained stable operation for over 50 cycles. The flexibility of the device was also validated, as it retained a consistent open-circuit voltage of  $\sim 1.32 \text{ V}$  under bending angles of  $120^\circ$ ,  $90^\circ$ , and  $60^\circ$  (Fig. S35).

Compared to conventional liquid-electrolyte ZABs, this rechargeable all-solid-state design offers distinct advantages, including compact design, mechanical flexibility, high power density, and improved operational safety.

## 5 Conclusions

This work develops a novel localized high-entropy engineering strategy to construct a high-performance  $\alpha\text{-Fe}_2\text{O}_3\text{@LHEO}$  electrocatalyst via spatially confining nanoscale Fe-Co-Ni-Zn-Mn high-entropy oxide within the  $\alpha\text{-Fe}_2\text{O}_3$  lattice. This unique design breaks the intrinsic bottlenecks of conventional iron-based OER electrocatalysts at the electronic and atomic levels,

delivering exceptional alkaline OER activity with greatly accelerated reaction kinetics, ultra-long operational stability under high current density, and outstanding performance in natural seawater-based rechargeable Zn-air batteries, far outperforming commercial noble metal benchmark catalysts.

Combined experimental characterizations and theoretical calculations reveal that the core of this performance breakthrough lies in the localized high-entropy effect: it induces lattice strain in  $\alpha\text{-Fe}_2\text{O}_3$ , tailors the electronic structure, and reduces the crystal field splitting energy to stabilize high-spin  $\text{Fe}^{3+}$ . These synergistic effects not only enhance charge transfer efficiency and optimize the adsorption/desorption of key oxygenated intermediates, but also switch the OER pathway from the conventional AEM to the more energetically favorable LOM, with the rate-determining step energy barrier reduced from 1.85 to 1.71 eV.

More importantly, the nanoscale localized high-entropy engineering proposed in this work breaks through the limitations of traditional bulk high-entropy material design and single modification strategies, establishing a new paradigm for the rational design of efficient and durable OER electrocatalysts using earth-abundant elements.

**Acknowledgements** This work was supported by the Shanghai Municipal Science and Technology Major Project, Shanghai Pilot Program for Basic Research-Shanghai Jiao Tong University (Grant No. 21T11400211), the National Natural Science Foundation of China (Grant No. 22579110), the Science and Technology Program of Tianjin (Grant Nos. 24YFZCSN00080 and 25ZYCGYS00020), the special basic research fund for central public welfare institute of China (Grant No. K-JBYWF-2024-QR-09) and the Doctoral Student Program of the Young S&T Talents Cultivation Project (CAST).

**Competing Interests** Zhen Huang is the Editor-in-Chief of *ENGINEERING Energy*, who was excluded from the peer-review process and all editorial decisions related to the acceptance and publication of this article. Peer-review was handled independently by the other editors to minimise bias.

**Electronic Supplementary Material** Supplementary material is available in the online version of this article at <https://doi.org/10.1007/s11708-026-1067-z> and is accessible for authorized users.

**Open Access** This article is licensed under a Creative Commons Attribution 4.0 International License, which permits use, sharing, adaptation, distribution and reproduction in any medium or format, as long as you give appropriate credit to the original author(s) and the source, provide a link to the Creative Commons license, and indicate if changes were made. The images or other third party material in this article are included in the article's Creative Commons license, unless indicated otherwise in a credit line to the material. If material is not included in the article's Creative Commons license and your intended use is not permitted by statutory regulation or exceeds the permitted use, you will need to obtain permission directly from the copyright holder. To view a copy of this license, visit <http://creativecommons.org/licenses/by/4.0/>

## References

- Mondal S, Das R C, Du Y, et al. Flexocatalytic hydrogen generation and organics degradation by nano  $\text{SrTiO}_3$ . *Advanced Science*, 2025, 12(23): 2500034
- Chu S, Wang Q. Climate change and innovative paths to a more sustainable future. *Frontiers in Energy*, 2024, 18(6): 717–726
- Miao D, Li J, Ren J, et al. Exploring the potential of Ni-based hydrogen evolution catalysts in anion exchange membrane water electrolyzer. *Advanced Materials*, 2026, 38(10): e20491
- Li Y, Qiu L, Tian R, et al. Chirality engineering of nanostructured copper oxide for enhancing oxygen evolution from water electrolysis. *Small*, 2024, 20(52): 2408248
- Tian R, Huang L, Li Y, et al. Spin-blockade effect of chiral multi-branch Au nanoparticles for mediating oxygen evolution reaction of electro-catalytic water splitting. *Chemical Engineering Journal*, 2025, 520: 165517
- Huang L, Wang T, Li Y, et al. Chiral helically grooved gold nanoarrows for concurrently enhancing oxygen and hydrogen evolution from electrochemical water splitting. *Science China Chemistry*, 2024, 67(11): 3767–3776
- Li J, Miao D, Guo X, et al. Sustainable zinc-air batteries: Innovations, challenges, and pathways to commercialization. *Small*, 2025, 21(49): e08482
- Chen D, Yu R, Yu K, et al. Bicontinuous  $\text{RuO}_2$  nanoreactors for acidic water oxidation. *Nature Communications*, 2024, 15(1): 3928
- Sha Q, Wang S, Yan L, et al. 10000-h-stable intermittent alkaline seawater electrolysis. *Nature*, 2025, 639(8054): 360–367
- Wang X, Xu L, Li C, et al. Developing a class of dual atom materials for multifunctional catalytic reactions. *Nature Communications*, 2023, 14(1): 7210
- Hong Q L, Xiao X, Ai X, et al. Organic interface enhanced electrocatalysis. *Chemical Society Reviews*, 2025, 54(21): 9849–9875
- Feng W, Chang B, Ren Y, et al. Proton exchange membrane water splitting: Advances in electrode structure and mass-charge transport optimization. *Advanced Materials*, 2025, 37(15): 2416012
- Song W, Xia C, Zaman S, et al. Advances in stability of NiFe-based anodes toward oxygen evolution reaction for alkaline water electrolysis. *Small*, 2024, 20(48): 2406075
- Li Y, Talib S H, Liu D, et al. Improved oxygen evolution reaction performance in  $\text{Co}_{0.4}\text{Mn}_{0.6}\text{O}_2$  nanosheets through Triple-doping (Cu, P, N) strategy and its application to Zn-air battery. *Applied Catalysis B: Environmental*, 2023, 320: 122023
- Niu H J, Ran N, Zhou W, et al. Synergistic atomic environment optimization of nickel-iron dual sites by Co doping and Cr vacancy for electrocatalytic oxygen evolution. *Journal of the American Chemical Society*, 2025, 147(3): 2607–2615
- Chen H, Liu Y, Zhang H, et al. Resolving the valence of iron oxides by resonant photoemission spectroscopy. *Journal of Physical Chemistry Letters*, 2025, 16(42): 10975–10981

17. Lou S, Wen G, Xu S, et al. Stabilizing the high spin cobalt atoms by local magnetic asymmetry in p-block metals-doped spinel  $\text{MnCo}_2\text{O}_4$  catalysts for efficient oxygen reduction. *Advanced Materials*, 2026, 38(2): e13681
18. Wang Y, Meng P, Yang Z, et al. Regulation of atomic Fe-spin state by crystal field and magnetic field for enhanced oxygen electrocatalysis in rechargeable zinc–air batteries. *Angewandte Chemie International Edition*, 2023, 62(28): e202304229
19. Li Y, Sun H, Ren L, et al. Asymmetric coordination regulating D-orbital spin-electron filling in single-atom iron catalyst for efficient oxygen reduction. *Angewandte Chemie International Edition*, 2024, 63(28): e202405334
20. Wang X T, Ouyang T, Wang L, et al. Redox-inert  $\text{Fe}^{3+}$  ions in octahedral sites of Co–Fe spinel oxides with enhanced oxygen catalytic activity for rechargeable zinc–air batteries. *Angewandte Chemie International Edition*, 2019, 58(38): 13291–13296
21. Ouyang T, Wang X T, Mai X Q, et al. Coupling magnetic single-crystal  $\text{Co}_2\text{Mo}_3\text{O}_8$  with ultrathin nitrogen-rich carbon layer for oxygen evolution reaction. *Angewandte Chemie International Edition*, 2020, 59(29): 11948–11957
22. Yang G, Zhu J, Yuan P, et al. Regulating Fe-spin state by atomically dispersed Mn–N in Fe–N–C catalysts with high oxygen reduction activity. *Nature Communications*, 2021, 12(1): 1734
23. Sun Y, Sun S, Yang H, et al. Spin-related electron transfer and orbital interactions in oxygen electrocatalysis. *Advanced Materials*, 2020, 32(39): 2003297
24. Ma S, Zhu Q, Zheng Z, et al. Nanosized  $\text{LiNi}_{1-x}\text{Fe}_x\text{PO}_4$  embedded in a mesoporous carbon matrix for high-performance electrochemical water splitting. *Chemical Communications (Cambridge)*, 2015, 51(87): 15815–15818
25. Dong H, Luo L, Zhou S, et al. Spin magnetic effect activate dual site intramolecular O–O bridging for nickel-iron hydroxide enhanced oxygen evolution catalysis. *Advanced Science*, 2025, 12(10): 2415525
26. Li N, Hadt R G, Hayes D, et al. Detection of high-valent iron species in alloyed oxidic cobaltates for catalysing the oxygen evolution reaction. *Nature Communications*, 2021, 12(1): 4218
27. Guerra Demingos P, Chen Z, Ni X, et al. Computational engineering of Non-van der Waals 2D magnetene for enhanced oxygen evolution and reduction reactions. *ChemSusChem*, 2025, 18(3): e202401157
28. Sun L, Wen K, Li G, et al. High-entropy alloys in catalysis: Progress, challenges, and prospects. *ACS Materials Au*, 2024, 4(6): 547–556
29. Yao Y, Dong Q, Brozena A, et al. High-entropy nanoparticles: Synthesis–structure–property relationships and data-driven discovery. *Science*, 2022, 376(6589): eabn3103
30. Ren J T, Chen L, Wang H Y, et al. High-entropy alloys in electrocatalysis: From fundamentals to applications. *Chemical Society Reviews*, 2023, 52(23): 8319–8373
31. Chida Y, Tomimori T, Ebata T, et al. Experimental study platform for electrocatalysis of atomic-level controlled high-entropy alloy surfaces. *Nature Communications*, 2023, 14(1): 4492
32. Wan Y, Wei W, Ding S, et al. A Multi-site synergistic effect in high-entropy alloy for efficient hydrogen evolution. *Advanced Functional Materials*, 2025, 35(5): 2414554
33. Ma Y, Ma Y, Wang Q, et al. High-entropy energy materials: challenges and new opportunities. *Energy & Environmental Science*, 2021, 14(5): 2883–2905
34. Zhao X, Cheng H, Wu L, et al. Sub-angstrom strain in high-entropy intermetallic boosts the oxygen reduction reaction in fuel cell cathodes. *Nature Communications*, 2025, 16(1): 7547
35. Zhang L, Zeng Y, Li H, et al. Engineering B-site configurational entropy in perovskite oxides for enhanced alkaline oxygen evolution reaction. *ChemSusChem*, 2026, 19(3): e70498
36. Xu Z, Wang Y, Zheng Z, et al. Electrochemical degradation of plastic waste coupled with hydrogen evolution in seawater using Rosette-like high-entropy oxides. *Advanced Science*, 2025, 12(35): e07023
37. Zhao Y, Wu J, Cao X, et al. High-entropy materials for water splitting: An atomic nanoengineering approach to sustainable hydrogen production. *Advanced Materials*, 2025, 37(36): 2506117
38. Chen J, Ma J, Huang T, et al. Iridium-free high-entropy alloy for acidic water oxidation at high current densities. *Angewandte Chemie International Edition*, 2025, 64(21): e202503330
39. Kohn W, Sham L J. Self-consistent equations including exchange and correlation effects. *Physical Review*, 1965, 140(4A): A1133–A1138
40. Kresse G, Furthmüller J. Efficient iterative schemes for ab initio total-energy calculations using a plane-wave basis set. *Physical Review B: Condensed Matter*, 1996, 54(16): 11169–11186
41. Kresse G, Joubert D. From ultrasoft pseudopotentials to the projector augmented-wave method. *Physical Review B: Condensed Matter*, 1999, 59(3): 1758–1775
42. Perdew J P, Chevary J A, Vosko S H, et al. Atoms, molecules, solids, and surfaces: Applications of the generalized gradient approximation for exchange and correlation. *Physical Review B: Condensed Matter*, 1992, 46(11): 6671–6687
43. Blöchl P E. Projector augmented-wave method. *Physical Review B: Condensed Matter*, 1994, 50(24): 17953–17979
44. Perdew J P, Burke K, Ernzerhof M. Generalized gradient approximation made simple. *Physical Review Letters*, 1996, 77(18): 3865–3868
45. Monkhorst H J, Pack J D. Special points for Brillouin-zone integrations. *Physical Review. B, Solid State*, 1976, 13(12): 5188–5192
46. Nørskov J K, Rossmeisl J, Logadottir A, et al. Origin of the overpotential for oxygen reduction at a fuel-cell cathode. *Journal of Physical Chemistry B*, 2004, 108(46): 17886–17892
47. Wang V, Xu N, Liu J C, et al. VASPKit: A user-friendly interface facilitating high-throughput computing and analysis using VASP code. *Computer Physics Communications*, 2021, 267: 108033
48. Jia C J, Sun L D, Yan Z G, et al. Single-crystalline iron oxide nanotubes. *Angewandte Chemie International Edition*, 2005,

- 44(28): 4328–4333
49. Huang H, Wang J, Liu Y, et al. Stacking textured films on lattice-mismatched transparent conducting oxides via matched Voronoi cell of oxygen sublattice. *Nature Materials*, 2024, 23(3): 383–390
50. Li C F, Xie L J, Zhao J W, et al. Interfacial electronic modulation by Fe<sub>2</sub>O<sub>3</sub>/NiFe-LDHs heterostructures for efficient oxygen evolution at high current density. *Applied Catalysis B: Environmental*, 2022, 306: 121097
51. Gao H, Shang L, Qian S, et al. Precise axial coordination tailors the spin state of single-atom iron for boosted oxygen reduction electrocatalysis. *Advanced Functional Materials*, 2026, early access, <https://doi.org/10.1002/adfm.202531932>
52. Zhou Z, Li B, Li J, et al. Strain-induced magnetic ordering unlocks spin-conserved catalysis in lithium-oxygen batteries. *Advanced Materials*, 2026, 72632(17): e72632
53. Lv Y, Fang Z, Zhou L, et al. Beyond volcano top of transition metal-based electrocatalysts triggered by spin state modulation. *Advanced Functional Materials*, 2026, 36(19): e20395
54. Shen G, Pan L, Zhang R, et al. Low-spin-state hematite with superior adsorption of anionic contaminations for water purification. *Advanced Materials*, 2020, 32(11): 1905988
55. Jiang J, Sun F, Zhou S, et al. Atomic-level insight into super-efficient electrocatalytic oxygen evolution on iron and vanadium co-doped nickel (oxy)hydroxide. *Nature Communications*, 2018, 9(1): 2885
56. Suntivich J, Gasteiger H A, Yabuuchi N, et al. Design principles for oxygen-reduction activity on perovskite oxide catalysts for fuel cells and metal–air batteries. *Nature Chemistry*, 2011, 3(7): 546–550
57. Yao T, Fu Q, Wang K, et al. Decoupling the effects of ruthenium sites and oxygen vacancies on the mechanism regulation of acidic water oxidation. *ACS Nano*, 2026, 20(2): 2510–2522
58. Zhong X, Wang H Y, Zhang C, et al. High-valence metal modulating lattice oxygen in high-entropy layered double hydroxides for enhanced oxygen evolution reaction. *Advanced Functional Materials*, 2025, 35(47): e72509
59. Pavlovic Z, Ranjan C, van Gastel M, et al. The active site for the water oxidising anodic iridium oxide probed through in situ Raman spectroscopy. *Chemical Communications*, 2017, 53(92): 12414–12417
60. Ma H, Chen W, Fan Q, et al. Regulating Sn self-doping and boosting solar water splitting performance of hematite nanorod arrays grown on fluorine-doped tin oxide via low-level Hf doping. *Journal of Colloid and Interface Science*, 2022, 625: 585–595
61. Wang Y, Chan Y S, Zhang R, et al. Insights into the contribution of oxygen vacancies on CO<sub>2</sub> activation for dry reforming of methane over ceria-based solid solutions. *Chemical Engineering Journal*, 2024, 481: 148360

## Author Biography



His research interest is focused on solar refineries and artificial

Baowen Zhou is currently an Associate Professor at the School of Mechanical Engineering, Shanghai Jiao Tong University. He received his Ph.D. from the Institute of Chemistry, Chinese Academy of Sciences, in 2016. He subsequently carried out postdoctoral research at McGill University, Canada (2017–2018), and at the University of Michigan, Ann Arbor, USA (2018–2020).

photosynthesis, green hydrogen and renewable fuels, biomass/waste valorization, and AI for energy. He has published about 100 papers in leading journals, including *Nature*, *Nature Catalysis*, *Nature Photonics*, *PNAS*, *Nature Communications*, *Angewandte Chemie International Edition*, *Chem*, *Energy & Environmental Science*, *Science Bulletin* and *ENGINEERING Energy*. Prof. Zhou is a committee member of the Carbon Dioxide Chemistry Committee of the Chinese Chemical Society and a committee member of the Chinese Energy Society. He also serves on the Editorial Boards of *Science Bulletin* and *Carbon & Hydrogen*, and on the Youth Editorial Boards of *ENGINEERING Energy* and *The Innovation*.